AIAA JOURNAL
Vol. 37, No. 6, June 1999

Image Processing for Interferometric Mie and Rayleigh Scattering Velocity Measurements

D. Bivolaru,* M. V. Ötügen,† A. Tzes,‡ and G. Papadopoulos§
Polytechnic University, Brooklyn, New York 11201

An image-processing method that is used in conjunction with a Fabry–Perot interferometer has been developed for time-resolved local velocity measurements in gas flows. The processing method is used to determine the Doppler shift in Mie or Rayleigh scattered light from the measurement volume. The method minimizes the adverse effects due to the drifting of laser frequency and interferometer alignment. The scattered light is mixed with unshifted light from the interrogation laser for reference before it is passed through the interferometer. The concentric, double-ring pattern images (from both the signal and the reference light) formed at the output of the interferometer are captured by a charge-coupled device camera and analyzed for free spectral range and Doppler shift simultaneously using an autocorrelation technique. Measurements have been made in the near field of a Mach 1.6 supersonic jet to determine the structure of the velocity field. Velocity data obtained using the present image analysis technique has been compared with those obtained using a direct analysis method in the same jet.

Introduction

NONINTRUSIVE, quantitative diagnostic techniques are needed in high-speed aerodynamics research to characterize flow parameters such as gas velocity, temperature, and density. Techniques are sought both for ground testing and for in-flight measurements. A desirable feature of a technique is the ability to obtain time-frozen measurements so that unsteady and turbulent features of the flow can be investigated. Developments are still needed in this area; however, several laser-based techniques have emerged in recent years that show promise for the future.

One of these techniques is interferometric Rayleigh/Mie scattering in which the spectral characteristics of the scattered light are analyzed using a Fabry–Perot interferometer.[1–5] In this technique, a narrow-line laser is used to interrogate a point or a two-dimensional plane in the flow. If Mie scattering is used, the spectral width of the scattered light is essentially the same as that of the incident laser light while the peak frequency is Doppler shifted by an amount that is a function of the velocity of the scattering particle as well as the optical configuration. However, the magnitude of this frequency shift is typically small for most aerodynamic applications (including supersonic flows), and accurate determination of it is difficult. If Rayleigh scattering is used, the line broadening and intensity of the scattered light from the molecules can be related to the gas temperature and density, providing additional information about the flowfield. One of the earlier attempts to use a Fabry–Perot interferometer to determine the local mean velocity is due to Eggins and Jackson,[1] who measured the Doppler shift due to the axial velocity in an underexpanded supersonic jet. The scatterers were solid particulates that occurred naturally during the jet expansion. They considered only the time-averaged velocity and used the interferometer in the scanning mode. The Rayleigh scattering-based method has been used to assess the viability of this method as a tool for rocket plume diagnostics[2] and for advanced short-takeoff/vertical landing model tests.[3] A scanning Fabry–Perot interferometer was used in these studies as well, and the data were postprocessed for time-averaged temperature and velocity. The method was later extended by capturing the two-dimensional Fabry–Perot images with a charge-coupled device (CCD) camera. With this approach, instantaneous velocity information was obtained in a supersonic wind tunnel[4] and at the exit of a supersonic jet.[5] In both cases, however, the acquired images were postprocessed after the experiments to determine the velocity.

Advanced image-processing methods must be employed to develop these interferometric techniques into robust, reliable, and routine diagnostic tools. First, fast, automated analysis of the Fabry–Perot interference patterns is necessary to obtain time-series data. Also, the image captured by the CCD camera can possess poor signal-to-noise characteristics, rendering the accurate determination of the Doppler shift difficult. Therefore, robust image-processing methods are needed to maintain levels of measurement resolution that are acceptable for quantitative results. Furthermore, because the Fabry–Perot alignment is highly sensitive to external conditions, such as temperature fluctuations and vibration (which tend to exist in both ground and in-flight tests), image analysis techniques that can take into account small degradations in instrument alignment are desirable.

In the present work, an image-processing method has been developed and tested for accuracy and reliability. The method depends on the linearization of the concentric circular interference rings from a planar Fabry–Perot interferometer and subsequent statistical analysis using a correlation method. The optical setup and analysis procedure allow for the determination of the Doppler shift independent of small drifts in the Fabry–Perot mirror alignment and the incident laser frequency, improving the versatility of the technique for use in practical applications.

Experimental Details

Fabry–Perot Interferometer

The Fabry–Perot interferometer is essentially made up of two partially transmitting mirrors placed parallel to one another inside a housing. In a plane Fabry–Perot interferometer, these mirrors are flat. If the space between the two partially reflecting mirrors is illuminated by a beam of monochromatic light entering through one mirror, the light will be transmitted through the other only when the optical path length between the surfaces is an integral number of the wavelength of the light. Therefore, the interferometer acts as a filter with a transmittance that is dependent on the wavelength of the light, the angle of the incident light beam relative to the surface normal of the mirrors, the refractive index of the medium between the two mirrors, and the distance between these mirrors. An in-depth theory of Fabry–Perot interferometers can be found in Ref. 6.

Presented as Paper 98-0511 at the AIAA 36th Aerospace Sciences Meeting, Reno, NV, Jan. 12–15, 1998; received March 14, 1998; revision received July 27, 1998; accepted for publication July 30, 1998.

*Graduate Assistant, Department of Mechanical, Aerospace and Manufacturing Engineering, Six Metrotech Center.

†Associate Professor, Department of Mechanical, Aerospace and Manufacturing Engineering, Six Metrotech Center. Senior Member AIAA.

‡Associate Professor, Department of Mechanical, Aerospace and Manufacturing Engineering, Six Metrotech Center.

§Research Scientist, Department of Mechanical, Aerospace and Manufacturing Engineering, Six Metrotech Center. Senior Member AIAA.

The most common way of using the Fabry–Perot interferometer is by moving one mirror relative to the other by piezoelectric means, thereby changing the distance between the two mirrors at a constant speed. In this scanning mode of operation, the output is monitored by a light sensor such as a photomultiplier tube, and the periodic transmission of light is related to the wavelength. In the scanning mode, time-resolved frequency characteristics of the light cannot be realized. An alternative to the scanning mode is to direct the incoming monochromatic light into the interferometer with a certain divergence angle and focus the output light of the interferometer by using a focusing (or fringe forming) lens. In this case, an interference pattern made up of a series of concentric bright rings of the transmitted light is formed at the focal plane of the lens. This image can be captured by a CCD camera[7] and subsequently analyzed to obtain the spectral characteristics of the light. Both the scanning and imaging modes of operation have been used in aerodynamic applications by Seasholtz et al.,[2] Kouros and Seasholtz,[3] Seasholtz et al.,[4] and Seasholtz.[5]

The free spectral range (FSR) of the interferometer, defined as the frequency range represented by the distance between two consecutive rings, is given by $\mathrm{FSR} = c/2Ln$. Here c is the velocity of light, n is the refractive index of the medium between the two mirrors (in the present study, $n = 1$ because room temperature air occupies the cavity of the interferometer), and L is the distance between the two mirrors. Larger FSR and, hence, a wider range of measurements can be obtained by reducing the distance between the two mirrors. However, this will also result in reduced measurement resolution. On the other hand, too large a value of L will not only make the interferometer alignment difficult but also will reduce the range of velocity that can be measured. Therefore, an optimum value of L has to be determined, taking into account both the expected velocity range and the optical configuration. In the present study, a plane Fabry–Perot interferometer was used in conjunction with a focusing lens at the output to form an interference pattern of concentric rings. The distance between the mirrors was selected as $L = 40$ mm, which yields a free spectral range of FRS = 3.75 GHz.

Experimental Setup

Figure 1 shows the optical arrangement for the present study. A narrow-line, pulsed Nd:YAG laser was used as the light source. The fundamental line of the laser is 1064 nm. The 532-nm second harmonic line of the laser, obtained by passing the infrared laser beam through a KDP crystal, was used for the experiments. The line narrowing was obtained by seeding the laser gain in the infrared through a diode laser. The linewidth at the 532-nm green line is estimated to be approximately 120 MHz (half-maximum, full width). In the experiments, the laser beam passed through the jet at a 45-deg angle. The scattered light from the probe volume was collected at 90 deg to the laser beam, as shown in Fig. 1. Therefore, the Doppler shift in the scattered light was proportional to the streamwise velocity component of the jet.

A small portion of the laser energy at the green line was extracted by a beam splitter before the beam formed the probe volume. This light, which served as the reference frequency during the measurements, was coupled into an optical fiber and collimated at the exit of the fiber, as shown in Fig. 1. A second beam splitter combined this reference light with the scattered light from the probe volume before passing both through the Fabry–Perot interferometer. The output of the interferometer was then focused on the CCD camera (using a 540-mm lens) where the concentric rings of the interference pattern were formed. The reference and measurement beams were aligned such that, when there was no flow, interference rings of the signal from the measurement volume coincide with those generated by the reference light.

Initially, Fabry–Perot images were obtained with double-ring patterns by slowly scanning one mirror of the interferometer and capturing two sets of rings (corresponding to two shots of the laser) on the CCD plane, simulating a Doppler-shifted light along with the reference. This was done to obtain high-signal-to-noise ideal images with which several candidate image analysis methods could be tested. Two personal computers were used for the present measurements. One computer controlled the operation of the CCD camera and received the images from the CCD camera, whereas the other controlled the operation of the laser and a ramp generator via an I/O board. The scanning of the Fabry–Perot mirror was achieved through the ramp generator. Each of the simulated images contained a different spacing between the sets of reference and measurement rings (simulating a different velocity) because the ramp speed was different for each case, whereas the exposure time on the camera was kept constant.

After verifying the robustness of the proposed image analysis technique through several simulated experiments as just described, actual experiments were carried out in a free supersonic air jet with an exit Mach number of $M = 1.6$. In this latter part of the investigation, the streamwise velocity was measured both on the jet axis and at several radial locations. The jet uses dried, compressed air from a large reservoir that is part of the Aerodynamic Research and Testing Facility at Polytechnic University. The exit diameter of the jet nozzle is $d = 8.9$ mm. Measurements were carried out for jet stagnation pressures of $P_0 = 5$ atm (jet A) and $P_0 = 3.38$ atm (jet B), corresponding to a slightly underexpanded jet and a slightly overexpanded jet, respectively. (Note that the stagnation pressure for the ideally expanded jet is 4.25 atm.)

Results

Simulated Fabry–Perot Images

Figure 2 shows three Fabry–Perot images captured by the CCD camera, simulating different velocities ranging from zero (Fig. 2a)

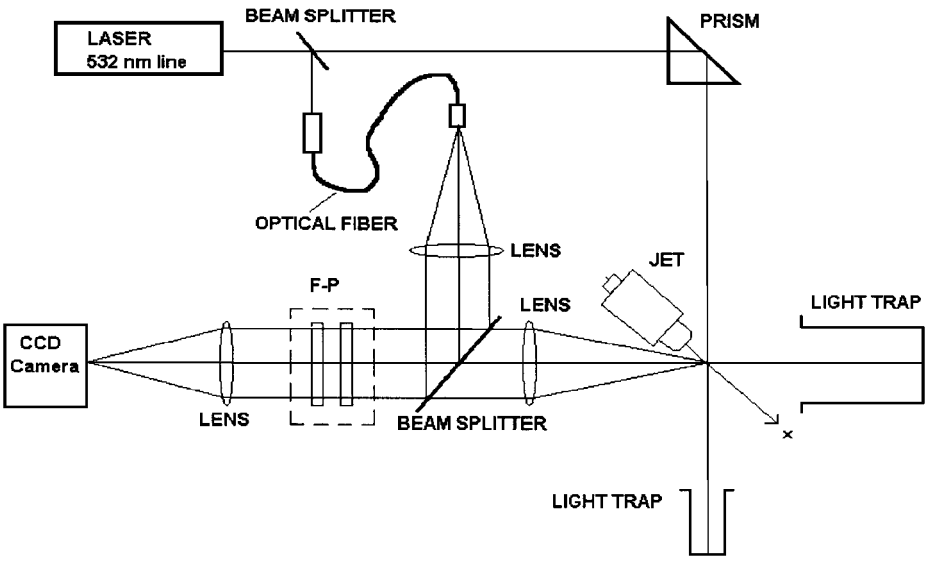

Fig. 1 Schematic of the optical system and the supersonic jet.

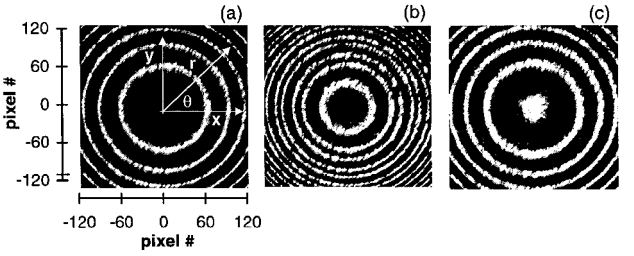

Fig. 2 Fabry–Perot images of the simulated flow.

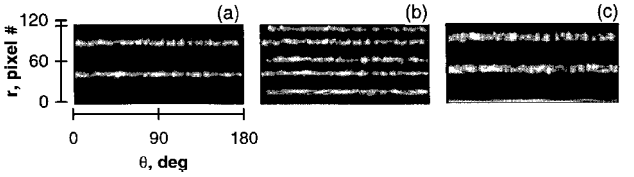

Fig. 3 Modified Fabry–Perot images in r–θ plane.

to the maximum velocity with the Doppler shift corresponding to nearly the FSR (3.75 GHz) of the system (Fig. 2c). In Fig. 2a, only one set of rings is present (corresponding to the reference or zero-velocity condition). Note that in the next image a second set of concentric rings forms. This second set represents the Mie/Rayleigh scattered light from the probe volume. As the measured velocity increases, this second set of fringes moves toward the center of the circles. Finally, in Fig. 2c, the Doppler shift is almost as large as the FSR, and the rings from the measurement volume nearly overlap the reference rings.

Image Processing for Velocity

The next objective is to process these images to determine the corresponding velocities. Note that each image contains its own reference along with the measurement. Therefore, with a proper image-processing scheme, the measured velocities should be independent of small drifts in the alignment of the interferometer and the frequency of the laser.

Software was developed to analyze the images shown in Fig. 2. Again, the objective of the processing was to obtain frequency shift in the measurement signal (and, hence, the velocity), given an image consisting of two sets of concentric circles (from a single Fabry–Perot) regardless of the position of their center on the CCD surface. All of the steps to be described were carried out by the dedicated software.

As a first step, the center of the circular rings was obtained. Then the circular rings were mapped onto the r–θ plane, as shown in Fig. 3. Obtaining Fig. 3 from Fig. 2 is a two-step process. Because of the linear pixel configuration of the CCD camera, the r values of the fringes in the raw r–θ plane have a minimum for $\theta = \pi/4$ and $3\pi/4$, and thus, the transformed rings are not straight lines. This was corrected by multiplying the r value for each pixel by an appropriate coefficient. The second corrective step has to do with a certain feature of the original Fabry–Perot image. As is characteristic of the Fabry–Perot interferometry, higher-order rings have smaller increments in radius that result in nonlinear spacing between the straight lines on the r–θ plane. The radius relationship between two consecutive rings is given by[6]

$$R_{p+1} \cong \sqrt{R_p^2 + (2f^2/k)} \tag{1}$$

where R is the radius of ring, subscript p is the fringe number, k is the order of interference, and f is the focal length of the fringe forming (or focusing) lens. A best fit was obtained for Eq. (1) using the actual images as follows:

$$R_{p+1} \cong \sqrt{1.05R_p^2 + 4155} \tag{2}$$

By using Eq. (2) as a compensation factor, the spacing of the fundamental (or reference) fringes was made constant, as shown in Fig. 3a. Each ring in Fig. 2 is represented by a straight fringe in Fig. 3 when the appropriate transformation is applied to r. Only the reference fringes exist in Fig. 3a, whereas the next image to its right has an extra set of rings whose distance to the reference rings characterizes the Doppler shift in the measurement signal. This distance increases with increasing velocity, and when the corresponding Doppler shift is as large as the FSR, the fringes corresponding to the actual signal coincide with the original reference fringes, as shown in Fig. 3c.

After investigating several statistical tools, based on correlation functions and Fourier transformations as possible tools for determining the average distance between the reference and the Doppler-shifted fringe in each image of Fig. 3, an autocorrelation-based technique was chosen for the analysis. The method is based on obtaining the correlation function of the two-dimensional images. Figure 4 shows the results of the method for the images in Figs. 3a and 3b. The correlation coefficient is obtained as follows:

$$R(i) = \frac{\sum_{n=1}^{N-i} I_n I_{n+i}}{\sum_{n=1}^{N} I^2 n} \tag{3}$$

where I_n is the intensity reading for entry n and N is the total number of entries as $N = r\theta$. The derivative of the correlation function for each case is shown in Fig. 5 to better identify the location of individual peaks. Note that each zero crossing reaching from the positive side of $R'(r)$ corresponds to a peak in Fig. 4. The dominant fringe spacings in Fig. 3 are identified in Fig. 5. The correlation

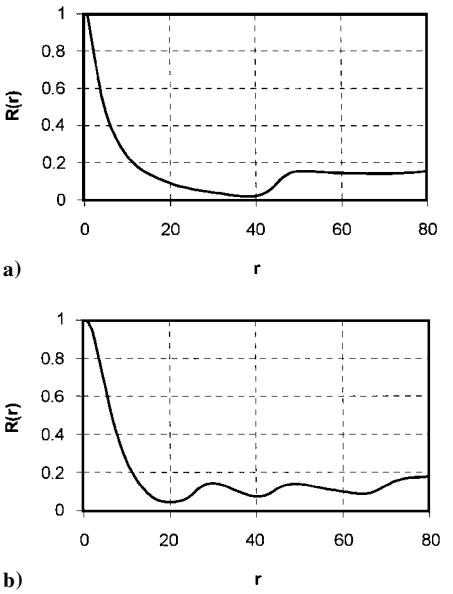

Fig. 4 Pseudocorrelation function for Fig. 3.

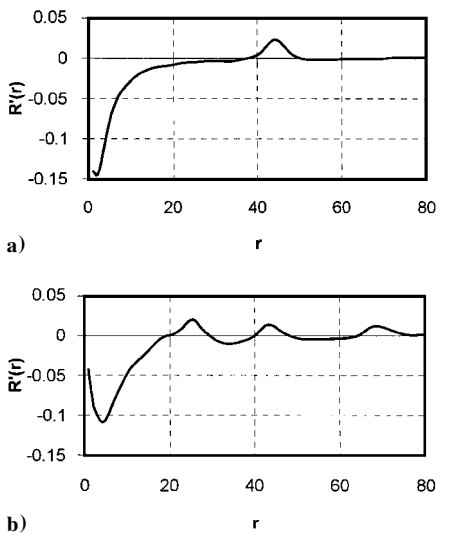

Fig. 5 Derivative of the correlation function in Fig. 4.

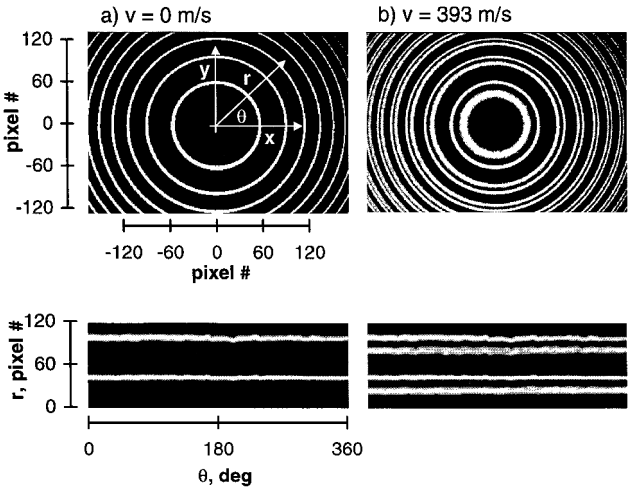

Fig. 6 Fabry–Perot images obtained in actual flow.

function for each case studied clearly shows a peak around $r = 50$, which corresponds to the FSR. In Fig. 4a, because there is no shift in measured frequency, the only peak is that for the FSR. In case b, however, a second peak is formed at $r = 26$, which corresponds to the shift frequency Δf. The third peak in Fig. 4b (and the corresponding additional zero crossing in Fig. 5b) observed at a higher value of r corresponds to a harmonic. In this case, because the harmonic has a larger r value than that for the FSR, it is easy to discriminate against during the determination process of the shift frequency. Note that in this case the shift frequency Δf is almost half of the FSR, and therefore, no additional peaks appear in the correlation with r smaller than that of the FSR. On the other hand, if Δf is significantly smaller or larger than half the FSR, an additional peak will appear (smaller than FSR), which will represent the complementary frequency (FSR $- \Delta f$). This indicates that, with the present technique, frequency shifts of only up to one-half of the FRS can be measured without ambiguities. This is also true for all spectral techniques (including fast-Fourier-transform-based methods) that may be employed for image analysis.

Measurements in Supersonic Jet

Next measurements were carried out in the supersonic jet facility described earlier. The laser beam and the collecting optics were situated such that the Doppler shift was directly proportional to the streamwise velocity (Fig. 1). Although planar measurements are possible using the present interferometric Rayleigh/Mie scattering technique as described earlier, the current measurements were essentially single point to obtain a better assessment of the image-processing method. A square section of the CCD output imaging a 1×1 mm plane of the actual flow was analyzed. The laser beam waist was focused to 1-mm diam at the probe. This rendered a cylindrical probe volume with a diameter and a length of 1 mm, thus providing a relatively high spatial resolution. Tests were carried out to determine statistically the uncertainty in the measured streamwise velocity. The uncertainty in time-averaged velocity is determined to be ± 20 m/s at 20:1 odds (95% confidence level).

Two representative images, one obtained in the jet and one with only the reference signal (corresponding to zero velocity), are shown in Fig. 6. Each of the images is obtained from a single shot of the laser. A slight broadening of the scattered signal from the probe is observed. This is perhaps due to partial molecular scattering along with a strong particulate scattering. Based on the estimated temperature of the jet in the measurement location, pure molecular scattering would have resulted in a much broader frequency (on the order of 2.5 GHz), nearly obscuring the FSR. Because particle scattering (both in the Mie and in the Rayleigh regimes) was expected to dominate, a narrow FSR of 3.75 GHz has been selected to maximize the measurement resolution. Indeed, surveys of the jets at different axial and radial locations showed that the scattering was dominated by particles. Near the jet exit and around the jet centerline, the scattering was predominantly in the Rayleigh mode (the condensation and subsequent formation of clusters of residual moisture in the supply air are very small), whereas at larger axial distances and near the edge of the jet, as the clusters agglomerate forming larger particles, Mie scattering came to dominate. The type of scattering was determined by observing the angular variation of the scattered light intensity from the probe volume. Because the incident laser light is vertically polarized, Rayleigh scattering maximizes when observed along the horizontal direction and vanishes along the vertical scattering direction. Any residual scattering observed along the vertical direction is Mie scattering. In any case, with the exception of very near the jet exit and far downstream ($x/d > 7.5$), the scattering was observed to be a combination of Mie and Rayleigh scattering. This makes measurements difficult because large variations in signal intensity are experienced from one location to the next. In Fig. 6, the renormalized r–θ maps of the Fabry–Perot images are also shown.

The pseudocorrelations corresponding to the processed images in Fig. 6 are shown in Fig. 7, and their derivatives are presented in Fig. 8. The FSR in both cases and the Doppler-shifted frequency for the case for $v = 393$ m/s are clearly seen as peaks in Fig. 7 and as zero crossings from positive in Fig. 8. In Fig. 8b, an additional zero crossing is observed between the velocity peak and the FSR, which corresponds to the complementary frequency discussed earlier. Indeed, the sum of the correlation distance r of the velocity and the complementary frequencies makes up for the FSR. In any

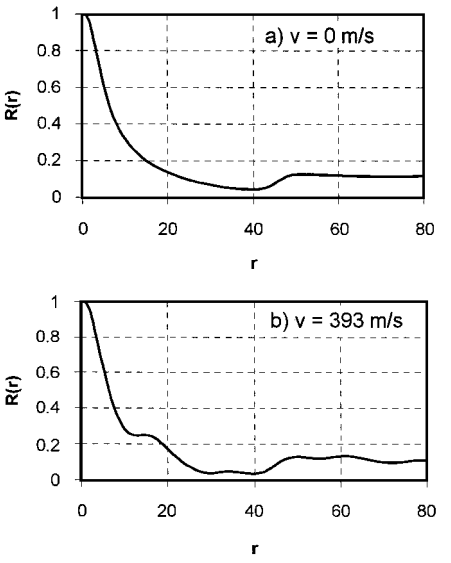

Fig. 7 Pseudocorrelation function for Fig. 6.

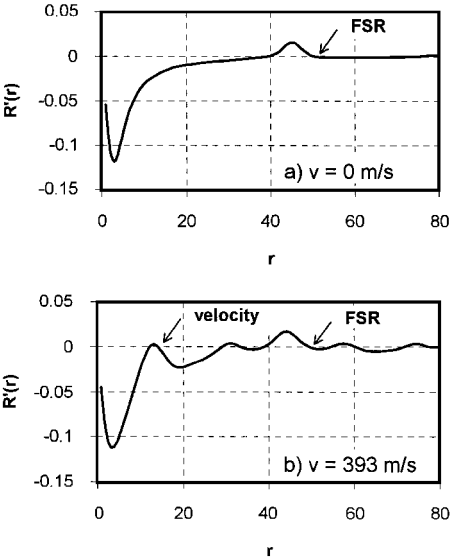

Fig. 8 Derivative of the correlation function in Fig. 7.

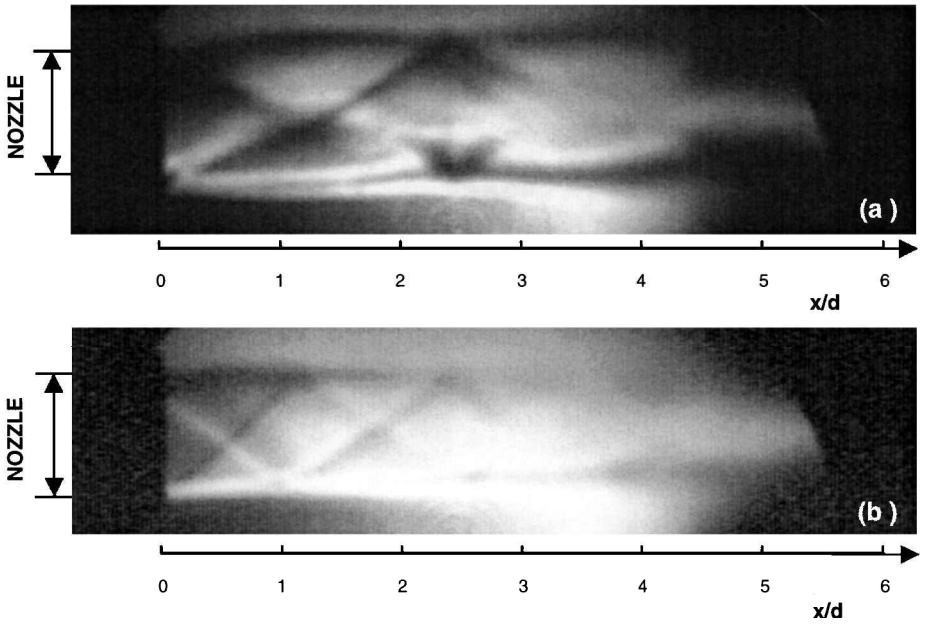

Fig. 9 Schlieren photographs of $M = 1.6$ supersonic jet: a) jet A, $P_0 = 5$ atm and $T_0 = 280$ K; and b) jet B, $P_0 = 3.38$ atm and $T_0 = 278$ K.

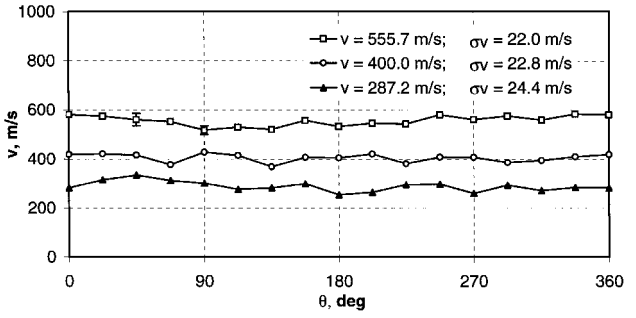

Fig. 10 Effect of θ on measured velocity.

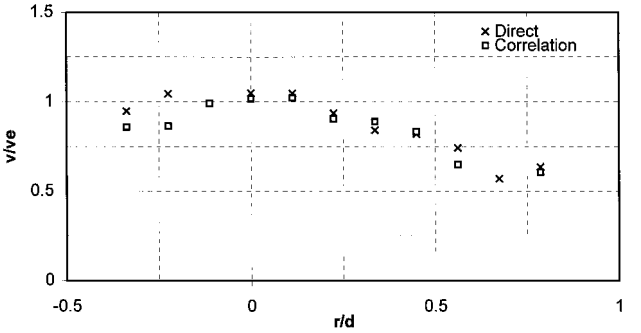

Fig. 11 Radial distribution of streamwise velocity at $x/d = 4.72$, jet A.

case, if the velocity range on the high end is limited to one-half of the FSR, the present technique provides fairly accurate time- and space-resolved velocity measurements.

Schlieren photographs of the Mach 1.6 jet under the measurement conditions are shown in Fig. 9. As is characteristic of a near-ideal expansion jet, the near field contains a series of shock cells that diminish in strength with increasing axial direction for both jet A and jet B. Figure 10 shows the variation of measured mean velocity with respect to the angle θ in the Fabry–Perot images. Each curve (set of data) in Fig. 10 is extracted from a single Fabry–Perot image obtained at a different measurement location close to the exit of jet A. Each data point represents the velocity obtained in a small angle range of $\Delta\theta = \pi/16$. For each $\Delta\theta$, 10 radial lines are used, and only the first two sets of interference rings are considered. The variation of the streamwise velocity v along the periphery of the image is relatively small. The average velocity around the periphery and the corresponding standard deviation are presented in Fig. 10. The standard deviation σv remains nearly constant, giving higher percent deviations for smaller velocities (almost 8.5% for $v =$ 287 m/s). As expected, this value is slightly larger than the uncertainty obtained when the whole image is used ($\pm$20 m/s). In addition to measurement uncertainty, actual variations of velocity within the imaged area can also contribute to σv. However, the analyzed image area is only 1 mm wide; hence, velocity variations within this field are not likely to occur. Thus, variations of velocity with angular position can be attributed solely to the image distortions and analysis accuracy. Obviously, the analysis of the entire image, rather than a small section of it, provides an improvement in accuracy. This additional benefit would not be available for two-dimensional measurements because measurements would have to be made in small subregions of the image plane. The error bars shown in the Fig. 10 represent the pixel resolution uncertainty if only a single radial line were used at each θ location. The velocity uncertainty due to pixel resolution for the first set of interference rings is estimated to be a minimum of 35.3 m/s (for $\theta = 0, \pi/2, 3\pi/2$, and 2π) and a maximum of 49.7 m/s (for $\theta = \pi/4, 3\pi/4, 5\pi/4$, and $7\pi/4$). Already, within each segment of $\Delta\theta = \pi/16$, using 10 radial lines provides an improvement in the velocity uncertainty.

Figure 11 shows the transverse distribution of the streamwise velocity normalized by the jet exit velocity v_e at $x/d = 4.72$ of jet A. Here two sets of data are shown, one obtained by using the present image analysis method and the other using a direct method. In the direct method, the interferometer is adjusted and a reference image is obtained (separately) immediately before the measurement for each data point. Each measurement image is then compared to its reference by using a peak detection method. This direct method provides a good standard for comparison, although it is not practical in actual measurements. The two sets of measurements are in good agreement. The velocity has a maximum at the centerline and progressively becomes smaller away from the jet axis, indicating the presence of a growing shear layer.

The shot-to-shot variation of streamwise velocity obtained in jet B using the present analysis method is shown in Fig. 12. The time-frozen velocities obtained at the location $x/d = 4$ and $r/d = 0.22$ are, again, normalized by jet exit velocity v_e. The corresponding mean velocity is represented by the straight line, and the relative rms of the velocity is about 7%. Based on the earlier uncertainty analysis, the contribution of the measurement uncertainty to the velocity rms at this location is about 3%. Therefore, the estimated turbulence intensity at this location is 4%. This level of turbulence is reasonable because, at $x/d = 4$, the flow has crossed several shock cells and is

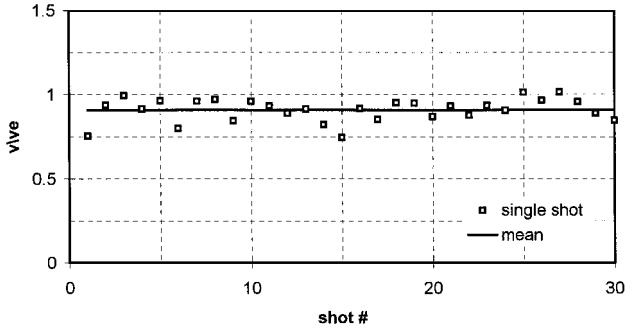

Fig. 12 Single-shot measurements of velocity, jet B.

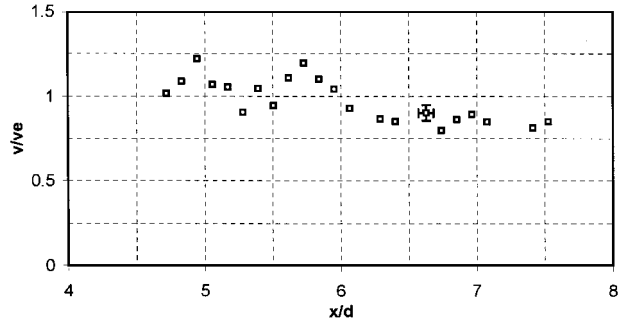

Fig. 13 Centerline mean streamwise velocity, jet A.

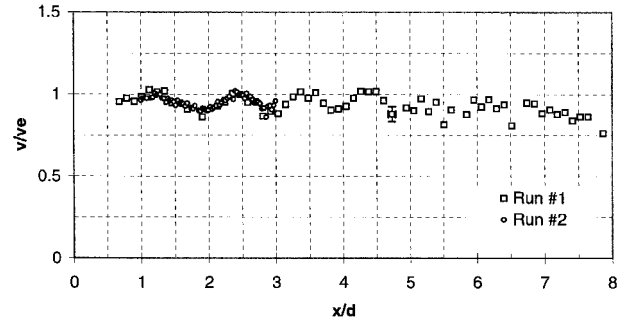

Fig. 14 Centerline mean streamwise velocity, jet B.

under the influence of the vortex dynamics in the surrounding shear layer.

The evolution of the normalized streamwise centerline velocity obtained using the present image analysis technique is shown in Fig. 13 for jet A and Fig. 14 for jet B. In both jets, the centerline velocity varies periodically with streamwise distance. However, these velocity fluctuations diminish with increasing x/d. The near field of the jets contains shock cells (Fig. 9) that serve as convergent–divergent passages through which the flow accelerates and decelerates in an alternating fashion. However, as the shear layer of the jet grows with entrainment and the shock structure becomes weaker with downstream distance, the variation of velocity also becomes smaller and eventually dies out. The amplitude of the velocity variations is larger for the underexpanded jet (jet A). To confirm the periodic behavior of the mean centerline velocity, a second set of data is obtained in the range $1 < x/d < 3$ for jet B, as shown in Fig. 14. This second set was obtained on a different day but under identical jet conditions, and the agreement between the two sets of data is within the measurement uncertainty (indicated in Fig. 14 with an error bar). Unfortunately, few direct velocity measurements in jet plumes are available in the open literature, and thus an independent verification of the present results is difficult. Chuech et al.,[8] Lepicovsky et al.,[9] and Panda[10] made centerline velocity measurements in the near field of sonic jets using laser Doppler anemometry (LDA). Chuech et al.[8] made measurements in both ideally expanded and slightly underexpanded jets, whereas Lepicovsky et al.[9] reported their jet to be ideally expanded. The results of these two studies do not show any periodic variation of velocity with streamwise distance. In contrast, the LDA measurements of Panda,[10] also made in an underexpanded sonic jet, show periodicity of the centerline Mach number with axial distance. Similar to the present results, the amplitude of the velocity variations diminish with streamwise distance. It is possible that the scatterers used in the LDA measurements in Refs. 8 and 9 may have been too large to follow the rapid periodic accelerations of the flow in this region due to particle inertia. In fact, the changing over of the scattering from small particles (Rayleigh regime) to larger Mie scattering particles with significant inertia may have contributed to the decay of the periodic velocity fluctuations with axial distance in the present study. Similar fluctuations in static pressure have been observed in ideally expanded as well as slightly underexpanded jets (measured and calculated; for example, see Ref. 11). Recent noninterferometric Rayleigh scattering measurements of Panda and Seasholtz[12] show that density also varies periodically in the streamwise direction in the near field of slightly underexpanded supersonic jets.

Finally, the radial distribution of the streamwise mean velocity for jet B is presented in Fig. 15. The local velocity is normalized by the centerline velocity v_0 at each streamwise station. These measurements have been obtained in a small range of x/d in an attempt to resolve velocity structure within one cell period. Indeed, each radial profile of the velocity is distinct. Only the profile at $x/d = 3.7$, corresponding to approximately the middle of a shock cell, exhibits a clear monotonic decay with increasing radial distance.

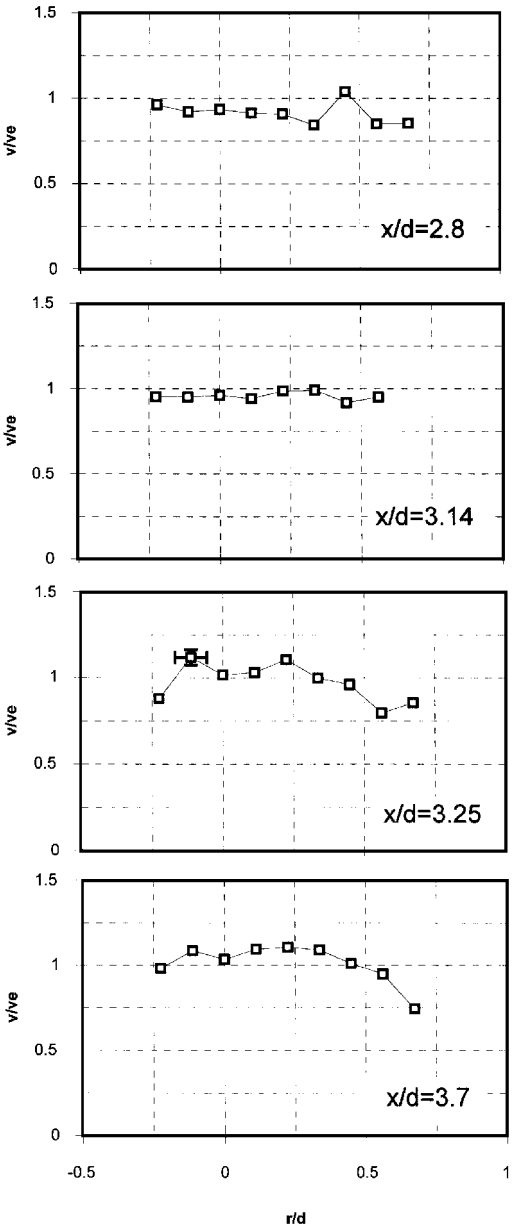

Fig. 15 Radial profiles of mean streamwise velocity, jet B.

Conclusions

The present Fabry–Perot-based Rayleigh scattering method offers improved velocity measurements because it can account for small drifts, over time, of both the laser frequency and the interferometer alignment. Both the reference laser line and the Doppler-shifted signal are simultaneously imaged as full sets of rings at each shot of the laser, enabling time-frozen measurements. For single-point measurements, the use of the whole imaging field leads to a further increase in the measurement accuracy, although this advantage would not be available for two-dimensional time- and space-resolved measurements. A relatively small FSR was chosen to obtain a high resolution in measured velocity. This was possible because the scattered signal was predominantly from particulates rather than from molecules (in both the Mie and Rayleigh regimes). For temperature measurements, however, the FSR needs to be set at a larger value, which will reduce the resolution in the measured velocity. Measurements in the $M = 1.6$ supersonic jets show that the centerline streamwise velocity varies periodically in the axial direction, but this periodicity diminishes at larger streamwise distances. The periodic fluctuations of the mean streamwise velocity are caused by the shock cells in the near field of the jet, which serve as convergent–divergent passages through which the flow alternatingly accelerates and decelerates. The amplitude of the velocity variations in the underexpanded jet is larger than in the overexpanded jet. The velocity profiles obtained in a single shock cell indicate a complex velocity structure in the near-field region of the supersonic jet.

Acknowledgments

The partial support for this research by NASA Lewis Research Center (with Richard G. Seasholtz as the Technical Monitor) is gratefully acknowledged.

References

[1]Eggins, P. L., and Jackson, D. A., "Laser-Doppler Velocity Measurements in an Under-Expanded Free Jet," *Journal of Physics D: Applied Physics*, Vol. 7, No. 14, 1974, pp. 1894–1906.

[2]Seasholtz, R. G., Zupanc, F. J., and Schneider, S. J., "Spectrally Resolved Rayleigh Scattering Diagnostics for Hydrogen–Oxygen Rocket Plume Studies," *Journal of Propulsion and Power*, Vol. 8, No. 5, 1992, pp. 935–942.

[3]Kouros, H. E., and Seasholtz, R. G., "Fabry–Perot Interferometer Measurements of Static Temperature and Velocity for ASTOVL Model Tests," *Proceedings of the Symposium on Laser Anemometry Advances and Applications*, edited by T. T. Huang and M. V. Ötügen, FED-Vol. 191, American Society of Mechanical Engineers, New York, 1994, pp. 65–70.

[4]Seasholtz, R. G., Buggele, A. E., and Reeder, M., "Instantaneous Measurements in a Supersonic Wind Tunnel Using Spectrally Resolved Rayleigh Scattering," *Proceedings of the International Symposium on Optical Science, Engineering and Instrumentation*, Society of Photo-Optical Instrumentation Engineers, Bellingham, WA, 1995.

[5]Seasholtz, R. G., "Single-Shot Spectrally Resolved UV Rayleigh Scattering Measurements in High Speed Flows," *Eighth International Symposium on Applications of Laser Techniques to Fluid Mechanics*, Centro de Termodinamika Aplicada e Mechanica dos Fluidos de Universitade Tecnica de Lisboa, Lisbon, Portugal, 1996.

[6]Vaughan, J. M., *The Fabry–Perot Interferometer. History, Theory, Practice and Applications*, Adam Hilger, Bristol, England, UK, 1989.

[7]Bunting, C. A., Carolan, P. G., Forrest, M. J., Noonan, P. G., and Sharpe, A. C., "CCD Camera as a Multichannel Analyzer for the Spectral and Azimuthal Resolution of Fabry–Perot Fringes," *Review of Scientific Instrumentation*, Vol. 59, No. 8, 1988, pp. 1488–1490.

[8]Chuech, S. C., Lai, M.-C., and Faeth, G. M., "Structure of Turbulent Sonic Underexpanded Free Jets," *AIAA Journal*, Vol. 27, No. 5, 1989, pp. 549–559.

[9]Lepicovsky, J., Ahuja, K. K., Brown, W. H., and Burrin, R. H., "Coherent Large-Scale Structures in High Reynolds Number Supersonic Jets," *AIAA Journal*, Vol. 25, No. 11, 1987, pp. 1419–1425.

[10]Panda, J., "Shock Oscillation in Underexpanded Screeching Jets," *Journal of Fluid Mechanics*, Vol. 363, May 1998, pp. 173–198.

[11]Dash, S. M., Wolf, D. E., and Seiner, J. M., "Analysis of Turbulent Underexpanded Jets, Part I: Parabolized Navier–Stokes Model, SCIPVIS," *AIAA Journal*, Vol. 23, No. 4, 1985, pp. 505–514.

[12]Panda, J., and Seasholtz, R. G., "Density Measurements in Underexpanded Supersonic Jets Using Rayleigh Scattering," AIAA Paper 98-0281, Jan. 1998.

R. P. Lucht and J. Seitzman
Associate Editors